O defect anchored Ru on BiOBr with nanoconfined structure for catalytic N$_2$ fixation

Yuzhou Xia [a,b], Xinghe Xia [c], Lu Chen [a], Ruowen Liang [a], Guiyang Yan [a,*], Shijing Liang [b,*]

[a] *Fujian Province University Key Laboratory of Green Energy and Environment Catalysis, Ningde Normal University, Ningde, Fujian 352100, PR China*
[b] *National Engineering Research Center of Chemical Fertilizer Catalyst, Fuzhou University, Fuzhou, Fujian 350002, PR China*
[c] *College of Chemistry, Fuzhou University, Fuzhou 350116, PR China*

ARTICLE INFO

ABSTRACT

Photocatalytic N$_2$ reduction using H$_2$O to produce NH$_3$ offers a promising alternative to the energy-intensive Haber-Bosch process. Nevertheless, its efficiency is hampered by the low solubility of N$_2$ in water, the high stability of N≡N and the competing H$_2$ evolution reaction (HER). In this study, we present a highly efficient nanohybrid system employing BiOBr nanoflowers with O defect as a platform for anchoring Ru. The designed nanohybrids exhibit a significantly higher NH$_3$ generation rate of 121.97 μmol g^{-1} h^{-1}, which is 6.1 and 2.8 times higher than that of pristine BiOBr-NS and Ru modified BiOBr without O defect, respectively. Experimental analyses and theoretical calculations reveal that the nanoflower structure with confined nano-space promotes the enrichment of N$_2$ on the catalyst, the synergistic O defects and Ru facilitate the selective adsorption and activation of N$_2$ and lower the energy barriers of the rate-determining *N-N to *N-NH step.

1. Introduction

NH$_3$ has become one of the most important chemical and industrial product in modern society for the application as fertilizer as well as clean energy carrier. In nature, only a few nitrogen-fixing microorganisms can directly convert nitrogen molecules into ammonia, which barely meets the substantial demand. Haber-Bosch nitrogen fixation process, the most widely adopted method for artificial ammonia synthesis, has made significant contributions to the progress of the whole human society [1,2]. However, this process relies on Fe-based catalysts under stringent reaction conditions (350–550 °C, 200–350 atm), consuming approximately 2% of the total annual energy supply and posing challenges to sustainable development [3]. A mild CO$_2$-free NH$_3$ synthesis route at lower temperature and pressure is highly desirable.

Photocatalytic N$_2$ reduction with H$_2$O into NH$_3$ has attracted tremendous interest as it can perform with solar energy as the driving force under ambient condition. However, the large dissociation energy of N≡N (941 kJ mol^{-1}) poses a substantial challenge to achieving a satisfied photocatalytic NH$_3$ evolution efficiency [4,5]. Moreover, the competitive redox potential of the H$_2$ evolution reaction (HER) with the N$_2$ reduction reaction (NRR) as well as the extremely low solubility of N$_2$ in H$_2$O make HER a strong competitor [6–11]. To address these

challenges, the design of photocatalysts for NH$_3$ synthesis should focus on simultaneously enhancing NRR and inhibiting HER.

Surface defect engineering technology has been recognized as an effective way to facilitate N$_2$ activation [12–18]. The coordination unsaturated atoms at defects sites with dangling bonds serve as effective active sites for N$_2$ transformation. Additionally, the introduced defects (such as O defect and Br defect) are rich in localized electrons, which can activate nitrogen molecules through π-back-donation into N$_2$ antibonding orbitals, thereby weakening the N≡N triple bond. This process leads to smoother hydrogenation of N$_2$ and formation of NH$_3$. In the last decades, various defect photocatalysts have been employed for N$_2$ reduction into NH$_3$, including TiO$_2$ [19,20], BiOBr [21,22], W$_{18}$O$_{49}$ [23], LDH [24] and Bi$_2$WO$_6$ [25]. Among which, layered BiOBr with [Bi$_2$O$_2$] slabs embedded in double slabs of Br$^-$ is of particular interest due to its inherent internal static electric field that promotes charge transfer [26,27]. However, ammonia yield rates over most reported systems remain unsatisfactory, possibly due to the preferential adsorption of H in the vicinity [28–30]. Given that nitrogen is a weak Lewis base due to its lone pairs of electrons, refining defects by associating them with metallic Lewis acid sites may enhance the selective binding of N$_2$ [31–35]. The unoccupied d-orbitals of the transition metal can accept the lone pair of electrons from dinitrogen (σ donation) thus facilitate the selective

---

* Corresponding authors.
E-mail addresses: ygyfjnu@163.com (G. Yan), sjliang2012@fzu.edu.cn (S. Liang).

activation of N_2 molecules. Especially, Ru species have triggered extensive interests in NRR because of their proper N_2 binding energy as well as high HER overpotential [36,37]. Theoretical calculations and experimental results have shown that the Ru atom as an active center not only accelerates N_2 adsorption and activation, inhibits *H adsorption and hydrogen precipitation side reactions, but also reduces the thermodynamic energy barrier of the rate-limiting step of N_2 fixation process (*N-N to *N-NH) [38]. Therefore, the synergistic of metallic Lewis acid sites Ru and defective BiOBr may offer an efficient approach for the selective adsorption and activation of N_2.

With regard to the low solubility and slow mass transfer rate of N_2 onto photocatalysts, various strategies have been adopted, including surface hydrophobic treatment and the use of non-aqueous solutions [39]. Given that NH_3 evolution involves a proton-coupled reduction process, proton scarcity may also restrict the N_2 reduction efficiency. Constructing porous materials represents a more appealing alternative, as the designed nanoconfined structure facilitates the enrichment of N_2 on the photocatalysts [40–44]. Moreover, the inner spatially interconnected pores enable rapid diffusion of N_2 to the active sites.

In light of the aforementioned analysis, we have fabricated porous nanoflower-like Ru-BiOBr hybrids, in which Ru is attached to the O defect of BiOBr, for efficient photocatalytic N_2 reduction. The synthesized samples demonstrate superior and stable photocatalytic performance in reducing N_2 into NH_3, with an optimal NH_3 evolution rate reaching 121.97 $\mu mol\ g^{-1}\ h^{-1}$. Experimental analyses and theoretical calculations reveal that the flower-like structure with a nanoconfined structure enhances reaction kinetics, while the synergistic active center of Ru refined O defect in BiOBr facilitates the selective chemisorption and activation of N_2.

2. Experimental

2.1. The preparation of BiOBr nanosphere

$Bi(NO_3)_3 \cdot 5\,H_2O$ (4 mmol) was first dissolved in 25 mL of ethylene glycol under vigorous stirring for 30 min. The resulting suspension was denoted as A. NaBr (4 mmol) was added to 25 mL of ethylene glycol and stirred for 30 min to create solution B. Subsequently, solution B was added drop by drop into suspension A at a rate of $0.2\ mL\ min^{-1}$. The resulting precursor solution was transferred into a 100 mL Teflon-lined autoclave and maintained at temperatures of 100 °C, 110 °C, 120 °C, 130 °C, and 140 °C for 10 h. After cooling down, the precipitate was centrifuged, collected, washed with absolute EtOH and deionized water several times, and finally dried under vacuum at 60 °C for 6 h. The synthesized material is labeled as BiOBr-NS.

2.2. The preparation of BiOBr nanoflower (BiOBr-NF)

$Bi(NO_3)_3 \cdot 5\,H_2O$ (4 mmol) was first dissolved in 25 mL of ethylene glycol under vigorous stirring for 30 min. The resulting suspension was denoted as A. NaBr (4 mmol) and PVP (0.05, 0.1, 0.15, and 0.2 g) were added to 25 mL of ethylene glycol and stirred for 30 min to create solution B. Subsequently, solution B was added drop by drop into suspension A at a rate of $0.2\ mL\ min^{-1}$. The resulting precursor solution was transferred into a 100 mL Teflon-lined autoclave and maintained at 120 °C for 10 h. After cooling down, the precipitate was centrifuged, collected, washed with absolute EtOH and deionized water several times, and finally dried under vacuum at 60 °C for 6 h. The synthesized material is labeled as BiOBr-NF-x.

2.3. The preparation of Ru-BiOBr-NF

Ru/BiOBr was prepared through an in-situ photoreduction process. Typically, 0.2 g of the obtained BiOBr nanoflower and $RuCl_3$ were added to 5 mL of methanol and 10 mL of H_2O. The mixture was subjected to ultrasonic treatment for 10 min and then purged with N_2 for 30 min.

Thereafter, the suspension was irradiated for 1 h using a 300 W Xe arc lamp. The final product was washed with EtOH and deionized water several times and dried under vacuum at 60 °C for 6 h.

2.4. The preparation of BiOBr

BiOBr was prepared using the same method as BiOBr nanospheres, except for using H_2O instead of ethylene glycol as the reaction solvent.

2.5. Characterization

The X-ray diffraction (XRD) patterns of the samples were measured using a Bruker D8 Advance X-ray diffractometer operating at 40 kV and 40 mA. The morphologies of the synthesized samples were investigated via field-emission scanning electron microscopy (SEM) (Hitachi SU8000, Japan) and transmission electron microscopy (TEM) images (FEI Talos F200s, USA). X-ray photoelectron spectroscopy (XPS) was measured using a VG Scientific ESCA Lab Mark II spectrometer. C 1 s at 284.6 eV was used for the calibration of the binding energies of tested elements. Electron paramagnetic resonance (EPR) measurements were performed using a Bruker A300 EPR spectrometer. For verifying O vacancies, the samples were vacuum-treated to remove surface adsorbate before testing, while the EPR signals for radicals were recorded with 2,2,6,6-tetramethyl-1-piperidinyloxy (TEMPO) as a trapping agent. UV–visible diffuse reflectance spectra (DRS) were recorded on a Varian Cary 500 UV–vis spectrophotometer. In-situ diffuse reflection infrared Fourier transform spectra (in situ DRIFTS) were studied using a Thermo IS 50 (Bruker, Germany). Electrochemical measurements were carried out using a ZENNIUM IM6 electrochemical workstation (Zahner, Germany). Pt plate and saturated Ag/AgCl electrode were used as the counter electrode and reference electrode, respectively. N_2 temperature programmed desorption spectrometry (N_2-TPD) was performed on an AutoChem II 2920 (Micromeritics) instrument equipped with a thermal conductivity detector. The ultraviolet-visible (UV) spectra were recorded on a Cary 60 UV–vis spectrophotometer (Agilent Technologies, USA). Ammonium cations were detected by ion chromatography on 930 Compact IC Flex (Metrohm).

2.6. Photocatalytic activity

The photocatalytic N_2 reduction reaction was performed under a 300-W Xe lamp in a top-irradiated quartz reactor. Typically, 10 mg of photocatalyst was dispersed in 50 mL of distilled H_2O under ultrasonic treatment for 10 min. The mixture was transferred into the reactor and vacuum-degassed for 30 min. Afterward, high-purity N_2 (>99.999%) was bubbled into the system. The degassing and bubbling process were repeated five times. Finally, the N_2 was bubbled for another 30 min before the light was turned on, and it continued to bubble throughout the reaction process. After the reaction, 10 mL of the reaction solution was collected and filtered with a 0.22 μm filter. The concentration of evolved NH_4^+ was determined using the salicylic acid analysis method by UV–vis spectrophotometry and ion chromatography. The calibration curve of NH_4^+ measured by UV–vis spectra and ion chromatography were displayed in Figure S1 and Figure S2.

2.7. Density functional theory (DFT) calculations

The calculations were conducted using the Vienna Ab initio Simulation Package (VASP). The Perdew-Burke-Ernzerhof (PBE) functional was employed to describe the exchange-correlation interaction. The core-valence electron interaction was treated with the projector augmented-wave (PAW) method. Van der Waals (vdW) corrections were applied using the Grimme approach (DFT-D3). The cutoff energy for the plane-wave basis sets was set to 400 eV. The energy criterion for iterative solutions of the Kohn-Sham equation was set to 10^{-5} eV. A three-layer 3×3 BiOBr (110) surface, with the bottom layer fixed, was used
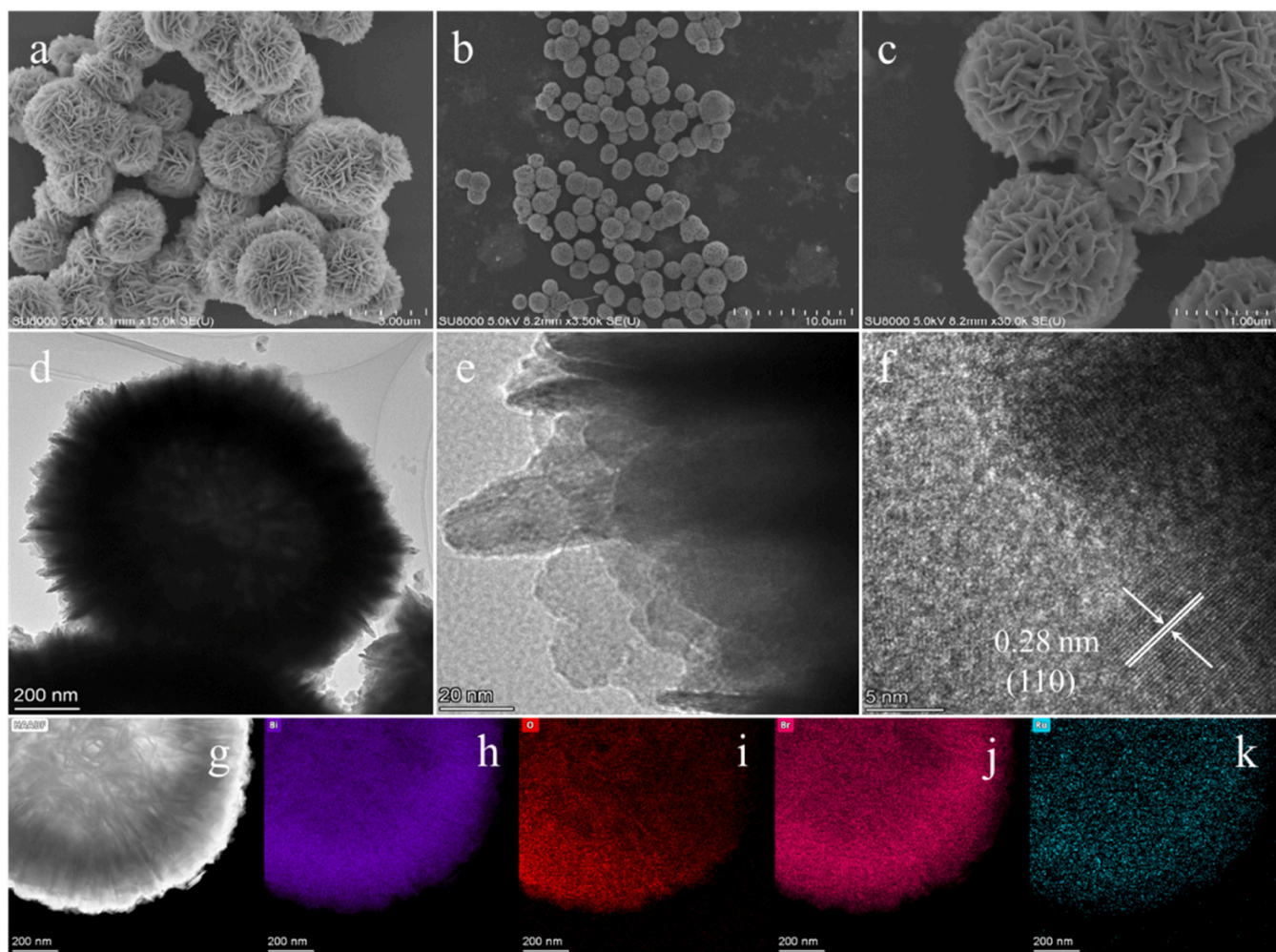
Fig. 1. SEM images of BiOBr-NF (a) and 1%Ru-BiOBr-NF (b, c), TEM of 1%Ru-BiOBr-NF (d-f) and the corresponding elemental mapping images (g-k).

for slab modeling. To prevent artificial interactions between periodic images, a vacuum layer with a width of 15 Å was added in the direction normal to the surfaces. An O atom was removed based on BiOBr (110) to simulate the oxygen vacancy (Vo-BiOBr). A Ru-Vo-BiOBr basal layer was constructed by replacing a Bi atom of V_O-BiOBr with a Ru atom. The Brillouin zone was sampled with a $2 \times 3 \times 1$ Gamma-center k-point mesh. All structures were relaxed until the residual forces on the atoms were less than 0.02 eV/Å.

3. Results and discussion

The crystal structures of the prepared samples are characterized by XRD. As shown in Figure S3 and Figure S4, all the obtained samples exhibit diffraction peaks at 10.9 °, 25.2 °, 31.7 °, 32.3 °, 39.4°, 46.3°, and 57.2°, corresponding to the (001), (101), (102), (110), (112), (200) and (212) crystal planes, respectively, matching well with the tetragonal BiOBr (JCPDS 09–0393) [45]. The introduction of Ru species has not significantly altered the XRD patterns of the composites.

The morphologies of the BiOBr samples are thoroughly invested using SEM. Figure S5 displays the SEM images of the samples synthesized at different temperature with ethylene glycol as the solvent. All of the samples exhibit a typical nanosphere structure. BiOBr nanosphere prepared at 100 °C consists of stacked nanorods. As the reaction temperature increased, the surface of the BiOBr nanospheres become smoother. The sample synthesized at 120 °C exhibits relatively uniform size with a diameter of 3.7 μm. When PVP is introduced during the synthetic process, the resulting BiOBr exhibits flower-like structures

(Figure S6). With the addition of 0.15 g PVP, BiOBr-NF (Fig. 1a) presents porous flower-like structures with a uniform size about 1–2 μm. The stacking of petals provides sufficient nanoconfined cavities, which may be beneficial for the surface enrichment of reactant (N_2) molecules. When Ru is decorated onto BiOBr-NF, the porous flower-like structures have been well maintained (Fig. 1b, c).

TEM measurements are performed to gain a more detailed information about the microstructure of BiOBr-NF and Ru-BiOBr-NF. As shown in Figure S7, the representative TEM image of BiOBr-NF shows porous flower-like and well-dispersed morphology. The petals are composed of thin nanosheets. A distinct 0.28 nm lattice fringe is observed in the HRTEM, corresponding to the (110) plane of BiOBr [46]. Ru-BiOBr-NF exhibits the typical nanoflower-like structure (Fig. 1d-f). The surface is clean with no visible particles in the HRTEM, suggesting that the loaded Ru species are amorphous and highly dispersed in the hybrids. HAADF-STEM and corresponding elemental mapping images confirms the coexistence and uniformly dispersion of Bi, O, Br and Ru in the photocatalyst, validating the successfully decoration of Ru species onto BiOBr with high dispersion (Fig. 1g-k).

XPS measurements are performed to elucidate the surface state and elementary microenvironment of the as-prepared samples. As illustrated in Fig. 2a, two spin-orbit doublets are deconvoluted for the Bi element in BiOBr, with binding energies at 164.5 eV and 159.3 eV, which are attributed to the 4 $f_{5/2}$ and 4 $f_{7/2}$ orbits of Bi(III) oxidation state, respectively [47]. In the case of the Bi spectrum in BiOBr-NF, the binding energy of Bi(III) decreased to 164.3 eV and 159.1 eV, suggesting low oxidation state Bi(III-x) species are evolved. This reduction in
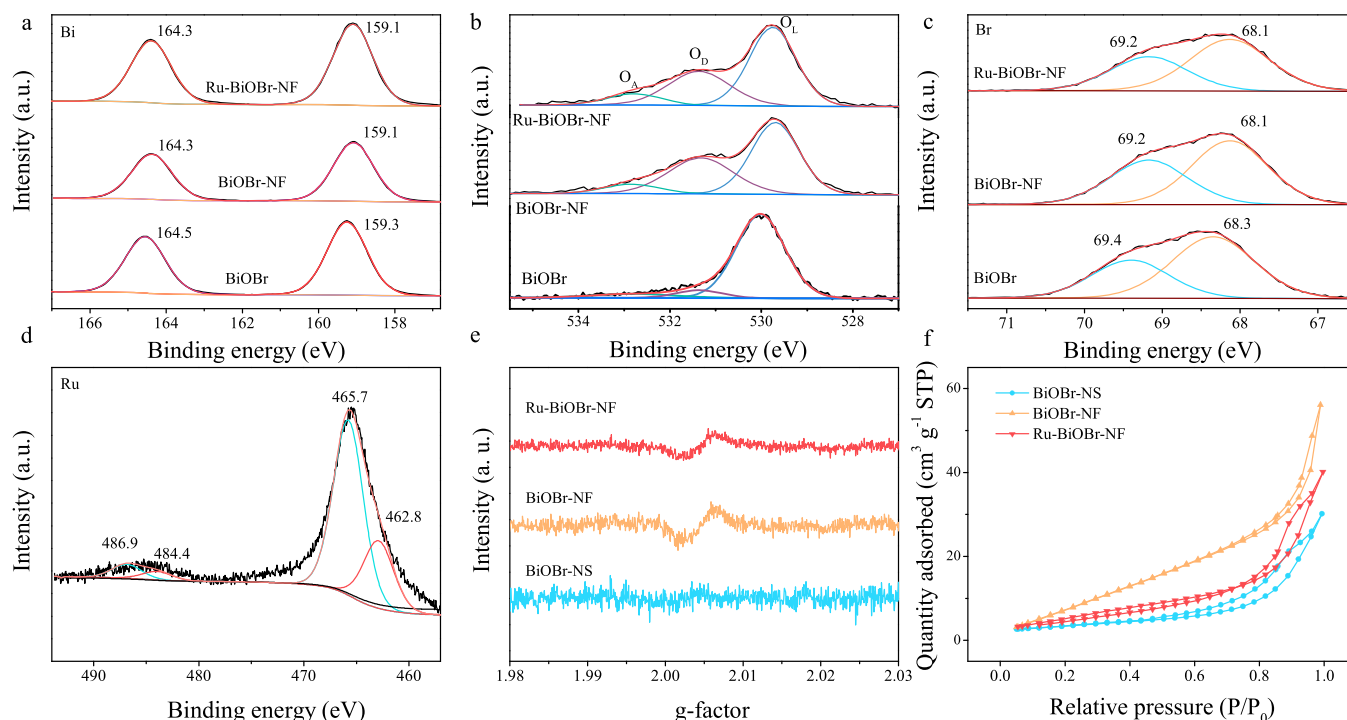
Fig. 2. XPS spectra of (a) Bi 4 f, (b) O 1 s, (c) Br 3d and (d) Ru 3p, EPR (e) and N_2 adsorption/desorption isotherms (f) of BiOBr, BiOBr-NF and Ru-BiOBr-NF.

oxidation state may be attributed to the removal of some terminal oxygen atoms due to the reducibility of ethylene glycol molecules during the solvothermal process. When Ru is deposited onto BiOBr-NF, the binding energies of Bi in Ru-BiOBr-NF show no shift compared to those of BiOBr-NF. As displayed in Fig. 2b, the O 1 s peak of BiOBr can be resolved into three peaks at 532.7 eV, 531.3 eV and 530.0 eV, corresponding to adsorbed oxygen (O_A), oxygen defect (O_D) and lattice oxygen (O_L), respectively [48]. As for BiOBr-NF, the peak position of O_A exhibits a slightly negative shift to 529.9 eV. The O_D peak in BiOBr-NF is significantly intensified when compare with BiOBr. The ratio of the O_D to the total O is about 37.1% for BiOBr-NF, which is higher than the proportion of O_D for BiOBr (7.5%), indicating that a higher amount of O defects is introduced. Ru-BiOBr-NF exhibit similar O 1 s spectrum to that of BiOBr-NF, except for a slightly decreased intensity of the O_D peak. It is interesting to see that the ratio of the O_D shows a regular decline trend with the increasing loading amount of Ru (Figure S8, Table S1). These results suggest that Ru may be deposited on the O defect.

The peaks of Br $3d_{5/2}$ and Br $3d_{3/2}$ are located at the binding energies of 68.3 eV and 69.4 eV (Fig. 2c), respectively, corresponding to the Br$^-$ species. The Br 3d peaks of BiOBr-NF and Ru-BiOBr-NF shift towards lower binding energy compared to that of BiOBr, indicating an increased charge density due to the local electrons of O defects. Regarding the Ru-BiOBr-NF, the high-resolution Ru 3p XPS spectrum in Fig. 2d can be deconvoluted into two pairs of characteristic peaks at 462.8 and 484.4 eV, 465.7 and 486.9 eV, which can be ascribed to the 3p3/2 and 3p1/2 of metallic and oxidized Ru (IV), respectively [49]. These results indicate that the Ru species in the sample are composed of mainly RuO_2 and a certain amount metallic Ru.

The existence of defects and the interaction between defects and the deposited Ru species are further invested via EPR (Fig. 2e). There is no signal in BiOBr prepared using H_2O as solvent, suggesting that the BiOBr is free of surface defect. In BiOBr-NF, a resonance peak located at g=2.003, ascribed to unpaired electrons, is clearly observed, suggesting the existence of abundant O defects [50,51]. FTIR spectrum of the fresh obtained BiOBr-NF has been investigated to reveal the possible formation mechanism of the O defects. As displayed in Figure S9, the characteristic peaks of ethylene glycol are observed in BiOBr-NF, suggesting

that ethylene glycol was adsorbed onto the surface of BiOBr. The possible adsorption configuration may via the bidentate hydrogen bonds between two alcoholic hydrogens in ethylene glycol and the lattice oxygen in BiOBr. Besides, a new peak emerged at 1136 cm^{-1}, which corresponds to the adsorbed glyoxal [52]. This result suggests that during the solvothermal process, ethylene glycol is oxidized into glyoxal (HO$(CH_2)_2$OH→OHC-CHO+4 H$^+$+4e$^-$). The desorbed H along with lattice oxygen formed H_2O, leaving O defects in BiOBr. Bi^{3+} is partially reduced into Bi$^{(3-δ)+}$ by e$^-$, which is in accordance with the XPS results. After Ru is deposited onto BiOBr-NF, the signal intensity of O defects decreased. These results suggest that Ru may be directionally anchored on the O defects of BiOBr.

The BET surface areas and pore size are determined through nitrogen adsorption analysis, as depicted in Fig. 2f and Figure S10. The specific surface areas of BiOBr-NS, BiOBr-NF and Ru-BiOBr-NF are determined to be 12.7, 38.7, and 25.6 m^2 g^{-1}, respectively. The pore volume of BiOBr-NF (0.06 cm^3 g^{-1}) is higher than that of BiOBr-NS (0.03 cm^3 g^{-1}). Additionally, the pore size of of BiOBr-NF (9.5 nm) is also larger than that of BiOBr-NS (8.7 nm). The increased surface area of BiOBr-NF is attributed to the loose flower-like structure with increased pore volume and pore size, which aligns with the SEM and TEM results. It is worth noting that the specific surface area and pore volume of Ru-BiOBr-NF are slightly decreased compared to those of BiOBr-NF, which may due to the partial collapse and blockage of the porous structure during the photo-depositing process.

The photocatalytic N_2 reduction experiments have been revalued with H_2O and N_2 as feedstocks. As shown in Fig. 3a, BiOBr exhibits a relatively low NH_3 generation rate of 7.23 μmol g^{-1} h^{-1}. For BiOBr-NS, the NH_3 yields increased to 20.12 μmol g^{-1} h^{-1}. In contrast, BiOBr-NF exhibits a significantly improved NH_3 evolution rate of 43.06 μmol g^{-1} h^{-1}, which can be attributed to the nanoconfined structure. Furthermore, the introduction of Ru onto BiOBr-NF leads to a further increase in photocatalytic NH_3 generation performance. As displayed in Fig. 3b, it is notable that all the Ru decorated BiOBr-NF reveal higher photoactivity than blank BiOBr-NF. With the increasing loading amount of Ru, the photocatalytic activities increase firstly and then decreased. 1%Ru-BiOBr-NF exhibits the highest NH_3 generation amount. The
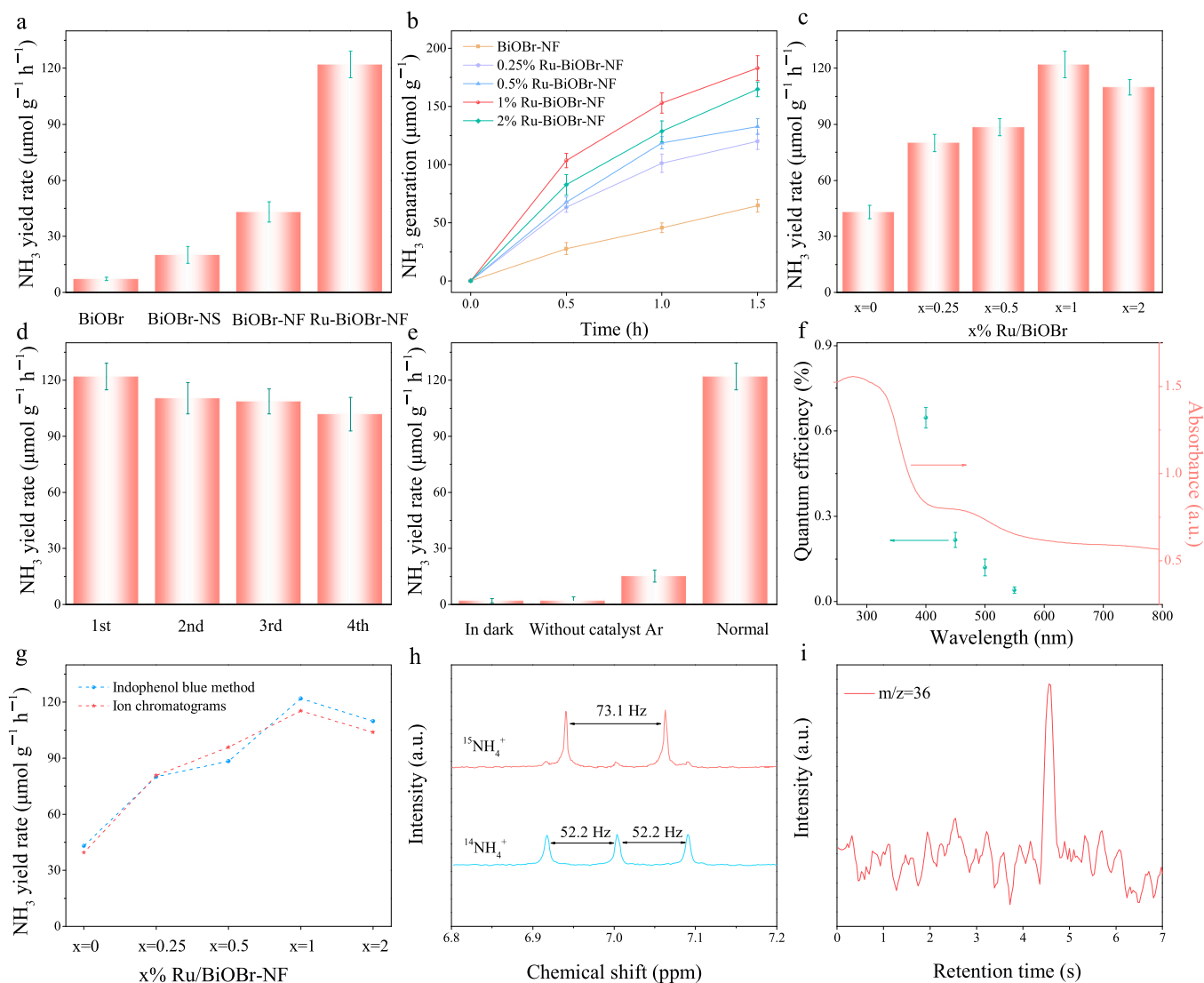
Fig. 3. Photocatalytic N_2 reduction performances of BiOBr-NS, BiOBr-NF and Ru-BiOBr-NF (a). Time course (b) and the yield (c) of NH_3 evolution in the photofixation of N_2 over BiOBr-NF with different Ru loading amounts. The cyclic tests of Ru-BiOBr-NF (d). Control experiments under different conditions (e). Apparent quantum efficiencies for N_2 photofixation over the Ru-BiOBr-NF (f). Comparison of two methods for determining ammonia concentration (g). The results of $^{15}N_2/^{14}N_2$ isotope labeling by ^1H NMR spectrum (h) and GC-Mass result of the evolved O_2 with $H_2^{18}O$ as reactant (i).

optimal rate of NH_3 generation reaches 121.97 μmol g^{-1} h^{-1}, which is 2.83 times greater than that of pure BiOBr-NF (Fig. 3c). These results strongly suggest that abundant active sites were introduced during the Ru modification which enhanced the N_2 photofixation reaction. Recycling experiments of Ru-BiOBr-NF suggest that the photocatalytic NH_3 evolution rate after four cycles remains 83.47% (Fig. 3d). XPS spectra of Ru-BiOBr-NF after the continuous 4 h tests of photocatalytic N_2 reduction have been recorded. As displayed in Figure S11, the Ru 3p and Br 3d peaks remain almost unchanged for the recovered sample when compared to its fresh counterpart. In regard to Bi 4 f, the two extra peaks at 163.1 and 157.9 eV in the recovered sample demonstrates the existence of reduction product of Bi^0, suggesting that partial of the surface Bi^{3+} is reduced by the photogenerated electron. While the recovered sample displays an intensified O_A which mainly due to the hydroxyl species and chemisorbed water during the photocatalytic process. Notably, the peak for O_D moved towards the higher binding energy direction after the reaction, consistent with the charge balance requirement. That is to say, the photoirradiation may increase the electronegativity of the O defects, which may also be beneficial for the chemisorption and activation of N_2 molecules. Since metallic Bi has been reported to be an effective active center for N_2 reduction [53,54], that

may be the reason for the steady N_2 generation rate for Ru-BiOBr-NF in the cycling tests.

To further explore the nitrogen source of the evolved NH_3, a series of controlled experiments have been conducted. As presented in Fig. 3e, a trace amount of NH_4^+ is detected when argon (Ar) is used instead of N_2 during the photocatalytic process with Ru-BiOBr-NF. No NH_4^+ is evolved when the reaction is performed in dark and without photocatalyst. The quantum efficiency of Ru-BiOBr-NF for the NH_3 generation under different monochromatic excitation was subsequently examined (Fig. 3f). The quantum efficiencies are calculated to be 0.64% at 400 nm, 0.22% at 450 nm, 0.12% at 500 nm and 0.04% at 550 nm. Moreover, the high-performances of the Ru loaded BiOBr-NF are also confirmed by ion chromatography (Fig. 3g). The evolved NH_3 concentrations detected by ion chromatography show no significant difference with those of indophenol blue method, validating the reliability of the experimental results. The prepared Ru-BiOBr-NF exhibits better performance than most of the reported works of photocatalytic N_2 reduction (Table S2). Ru-loaded BiOBr without O defects (1%Ru/BiOBr) has also been prepared for comparison. As shown in Figure S12, the NH_3 evolution rate is 43.5 μmol g^{-1} h^{-1}. These results indicate that the nanoconfined structure and Ru-O defects active units play crucial and synergistic roles in
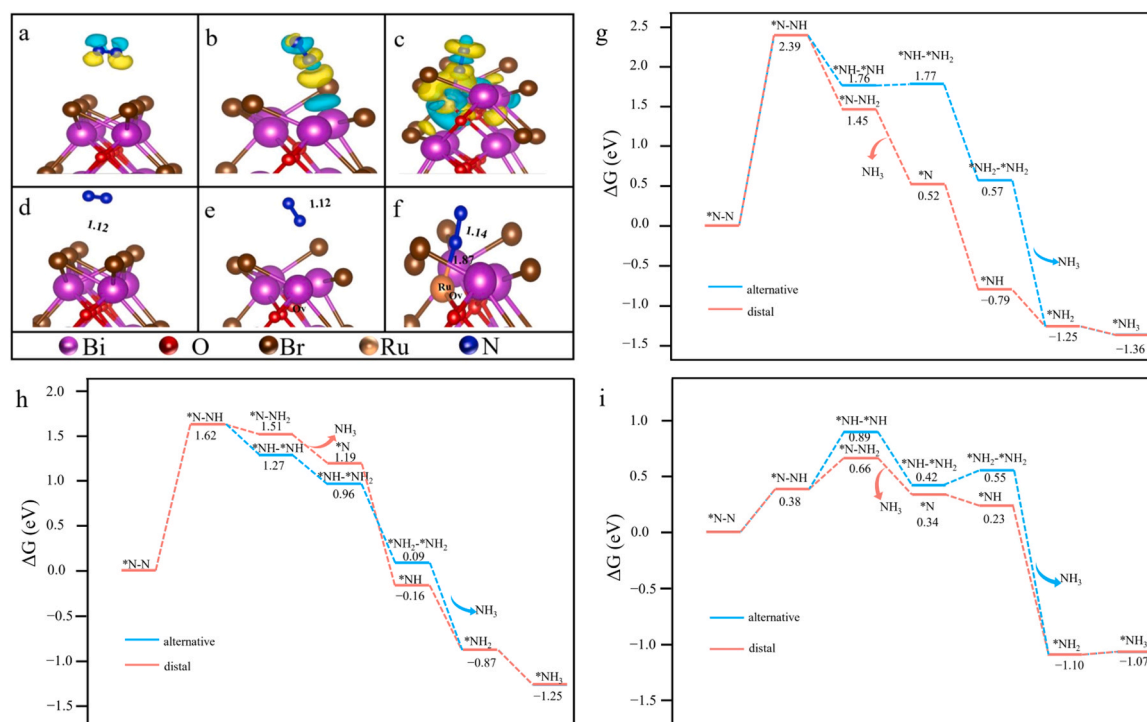
Fig. 4. Differential charge densities of BiOBr (a), BiOBr-NF with O defects (b) and Ru-BiOBr-NF (c) with adsorbed N_2 (color coding consists of blue for charge loss and yellow for charge gain); Structures of N_2 adsorbed on BiOBr (d), BiOBr-NF with O defects (e) and Ru-BiOBr-NF (f); Gibbs free energy (ΔG) diagrams of N_2 photoreduction to NH_3 through different paths over BiOBr (g), BiOBr-NF with O defects (h) and Ru-BiOBr-NF (i).

photocatalytic N_2 fixation. Isotope labelling experiments were performed with $^{15}N_2$ as the reactant under the same conditions as the $^{14}N_2$ experiments. The results from ^1H nuclear magnetic resonance (NMR) measurements suggest that typical triplets of NH_4^+ are detected when $^{14}N_2$ is used, while doublets of $^{15}NH_4^+$ with a coupling constant of 73.1 Hz are detected when $^{15}N_2$ is employed (Fig. 3h). These results confirm that the evolved NH_3 indeed originates from N_2 through the photocatalytic reduction process. To gain insight into the oxidation half-reaction, N_2 reduction reactions were performed in a batch reactor with N_2 and $H_2^{18}O$ as the reactants. After reacting for 2 h, 0.5 mL of the produced gas was collected with a syringe and analyzed by GC-Mass. As displayed in Fig. 3i, $^{18}O_2$ ($m/z = 36$) is detected as the dominant product. Moreover, the photocatalytic O_2 evolution activity of the catalyst has been investigated. When the experiments were performed with the as-obtained photocatalysts in pure H_2O, no O_2 was detected. The possible reason may due to the low O_2 evolution amount which is below the chromatographic detection limit. When $AgNO_3$ was introduced as electron capture agent, all of the prepared catalysts exhibit photocatalytic O_2 generation activity (Figure S13). These results strongly suggest that the half reaction of H_2O oxidation occurs in the photocatalytic process.

DFT calculations have been performed to get deeper understanding of the interaction between N_2 and Ru-BiOBr-NF as well as the photocatalytic N_2 reduction process. The complete layer of the model BiOBr is displayed in Figure S14. As displayed in Fig. 4a-c, the charge differential density results reveal that the significant electron transfer between Ru-BiOBr-NF and adsorbed $*N_2$ is observed. Charge density difference plots indicate that, upon adsorption, the adsorbed N_2 is prone to interact with Ru. The charge between Ru and N increases and the charge between N-N decreases, suggesting that the unoccupied d-orbitals of Ru can accept the lone pair of electrons from dinitrogen thus facilitate the selective activation of N_2 molecules, resulting in the formation of the N-Ru bond with the length of 1.87 Å and the notable weakening of the N≡N triple bond. As such, the N-N bond length would be elongated from 1.12 Å to 1.14 Å (Fig. 4d-f). As for BiOBr-NF, N_2 molecules can also be well adsorbed on

the O defects, with a relatively inferior intensity than Ru-BiOBr-NF. For N_2 adsorption on BiOBr, no significant charge transfer is observed. The adsorption energies of N_2 on pristine BiOBr, BiOBr-NF and Ru-BiOBr-NF are calculated to be −0.08, −0.33 and −0.55 eV, respectively. These findings unveil that the refining of O defects by Ru is beneficial for the adsorption and activation of N_2 molecules. Moreover, the overall reaction mechanism of N_2 reduction reaction (NRR) on the as-prepared samples, where both distal and alternating reaction pathways have been carefully investigated. For BiOBr (Fig. 4g), the process of $*N-N$ to $*N-NH$ has the highest energy barrier (2.39 eV) of all steps. The free energy change (ΔG) for the formation of $*N-NH_2$ and $*N-NH$ are −0.63 eV and −0.94 eV, respectively. Therefore, N_2 molecule is more inclined to be hydrogenated through the distal pathway. As for BiOBr-NF (Fig. 4h), it is found that both the distal and alternating reaction pathways exhibit the same rate-determining step of $*N-N$ to $*N-NH$ with the energy barriers of 1.62 eV. The relatively decreased energy barrier compared to BiOBr suggests the introduction of O defects facilitated the hydrogenation of N_2 molecules. After the modification of Ru (Fig. 4i), ΔG from $*N-N$ to $*N-NH$ (0.38 eV) is much lower than that from $*N-NH$ to $*NH-*NH$ (0.51 eV), indicating that the photocatalytic nitrogen fixation over Ru-BiOBr-NF experienced the distal pathway. The conversion of $*N-N$ to $*N-NH$ is the determining step with an energy barrier of 0.38 eV, which is much lower than the energy barrier of the determining step on BiOBr-NF. Overall, the above calculations indicated that the introduction of the Ru in BiOBr with O defect could create active sites. In addition, the stronger charge redistribution at Ru and O defects units greatly reduced the energy barriers of the rate-limiting step, thus further facilitating the activation of N_2 and hydrogenation reaction.

In-situ diffuse reflectance infrared Fourier transform spectroscopy (in-situ DRIFTS) has been conducted to investigate the potential N_2 reduction process. As shown in Figure S15a, the spectrum for BiOBr recorded at different times remain almost unchanged, suggesting the weak interaction between N_2 and BiOBr as well as the sluggish N_2 reduction reaction kinetics. As for BiOBr-NF (Figure S15b), the peak at 1637 cm^{-1} emerges due to the adsorbed N_2 on the surface of catalysts
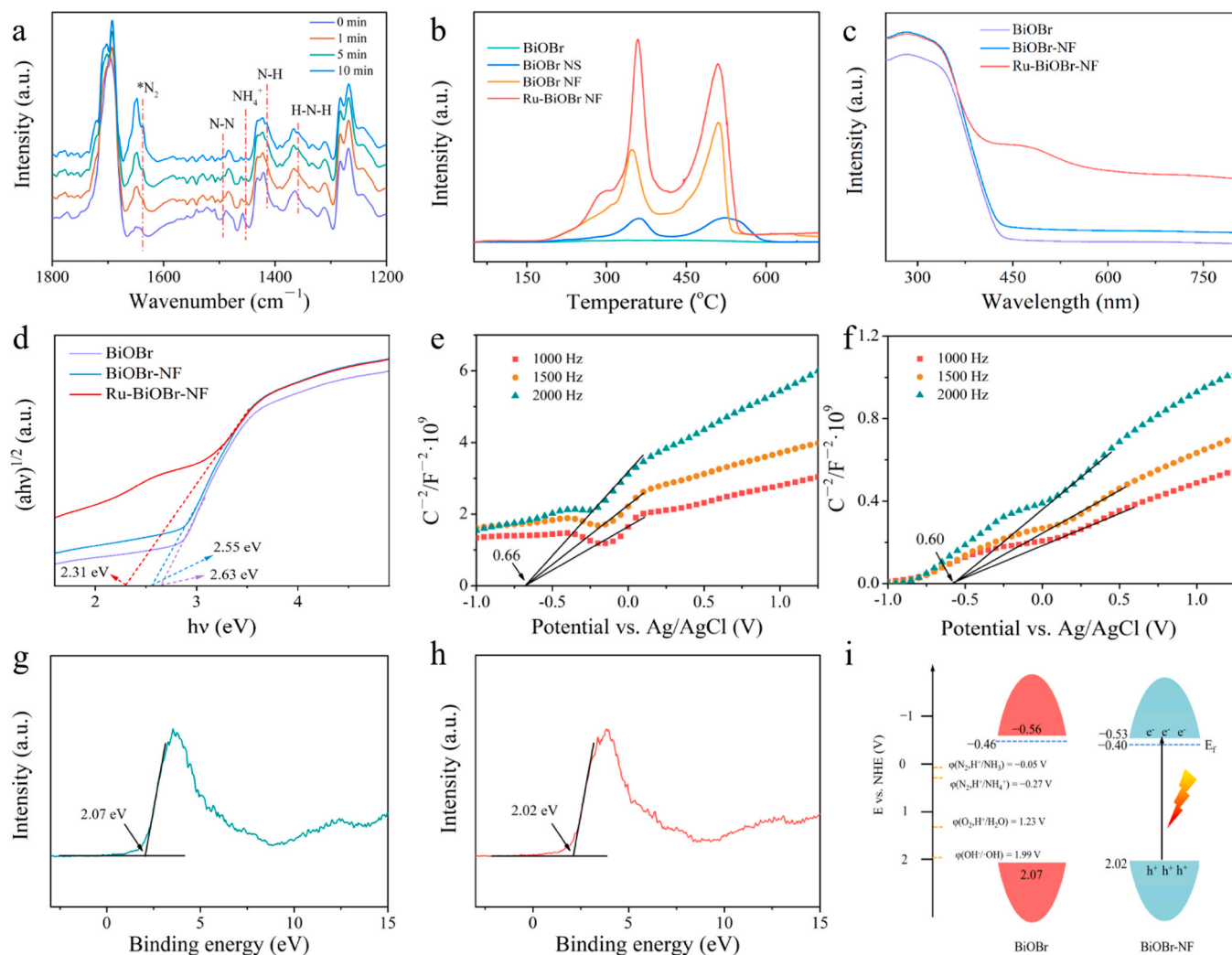
Fig. 5. In-situ DRIFTS spectra of Ru-BiOBr-NF (a). N_2-TPD profiles of the as-prepared samples (b). DRS (c) and the corresponding Tauc plots (d) of the as-perpared samples. Mott-Schottky plots of BiOBr (e) and BiOBr-NF (f). VB XPS of BiOBr (g) and BiOBr-NF (h). Schematic illustration of the band structure of BiOBr and BiOBr-NF (i).

[55]. This result suggests that the existence of O defects contribute to the enhancement of N_2 chemisorption, which is in accordance with the CO_2-TPD result. For Ru-BiOBr-NF (Fig. 5a), the peak ascribed to *N_2 is also observed. Moreover, the activation of N_2 lead to the appearance of new peaks at 1358 cm^{-1}, 1415 cm^{-1} and 1490 cm^{-1}, corresponding to the vibrations of H-N-H, N-H and N-N bending in the intermediate products, respectively [56–58]. The absorption band at 1453 cm^{-1} is account due to the N-H symmetric deformation vibration of the adsorption product NH_4^+, suggesting that the synergistic O defects and RuO_2 enhanced adsorption of N_2 and conversion of N-H to NH_3. Overall, O defects are beneficial for the chemisorption of N_2 molecules, while RuO_2 adjusts electronic structures of BiOBr-NF, leading to the promotion of N_2 activation and lowering of the energy barriers of the rate-determining *N-N to *N-NH step.

N_2-TPD has been measured to assess the N_2 adsorption capacity of the prepared photocatalysts. As illustrated in Fig. 5b, the N_2 desorption signal of BiOBr is negligible, suggesting a weak interaction between N_2 and BiOBr. For BiOBr-NS, two desorption peaks at 360 °C and 523 °C are detected. When the porous BiOBr-NF is tested, the N_2 desorption peaks are significantly intensified, confirming a much-improved N_2 affinity. These results reveal that the designed porous structure with confined micro-space is beneficial for the enrichment of N_2 molecules at the reaction sites. In the case of Ru-BiOBr-NF, the peak areas for both physical and chemical desorption are significantly increased, favoring substantial

enhancement of N_2 adsorption and leading to improved electron distribution symmetry. This, in turn, weakens the N≡N bond and benefits N_2 activation.

The photoabsorption performance have been evaluated by DRS. As displays in Fig. 5c, BiOBr exhibits a distinct absorption edge at 433 nm. In the case of BiOBr-NF, the absorption edge shows a red-shift to 438 nm, possibly attributed to the presence of "sub-band" induced by O defects. An intensified absorption in the visible region is observed in Ru-BiOBr-NF when compared to BiOBr. The Tauc curve (Fig. 5d) reveals that the band gap energies of BiOBr and BiOBr-NF are 2.63 eV and 2.55 eV, respectively. Mott-Schottky tests are performed to investigate the band structure of BiOBr and BiOBr-NF. The Mott-Schottky plots have been remeasured at the frequencies of 1000 Hz, 1500 Hz and 2000 Hz. As displayed in Fig. 5e-f, the positive slope implies the typical n-type semiconductor properties of the prepared BiOBr and BiOBr-NF. The calculated flat-band (E_f) potentials of BiOBr and BiOBr-NF are −0.66 V and −0.60 V (vs. Ag/AgCl, pH=7), respectively. According to the equation $E_{NHE} = E_{Ag/AgCl} + E^0_{Ag/AgCl}$, the E_f of BiOBr and BiOBr-NF are calculated to be −0.46 V and −0.40 V (vs. NHE, pH = 7), respectively. Considering that the E_f is about 0.1–0.3 eV more positive than the conduction band minimum (CBM) for n-type semiconductor, the valence-band (VB) XPS of the synthesized the have been measured to determine the band structures of the samples. As presented in Fig. 5g-h, the the VB edges of BiOBr and BiOBr-NF are estimated to 2.06 eV and
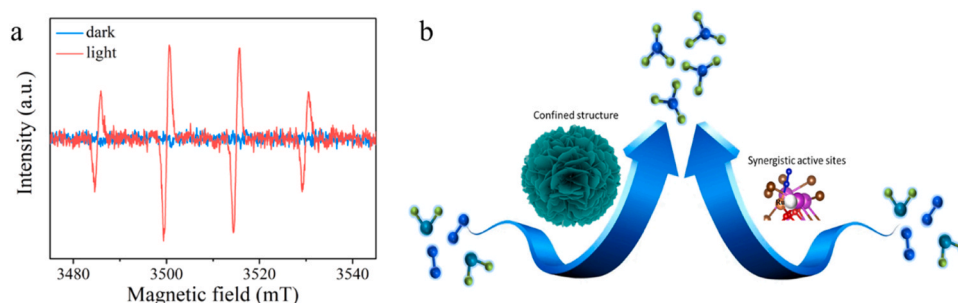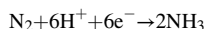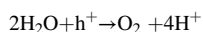
Fig. 6. EPR spin-trapping spectra for DMPO-•OH (a) and schematic diagram of nitrogen reduction reaction for Ru-BiOBr-NF (b).

2.02 eV. According to the results of band gaps and valence band, the conduction band of BiOBr and BiOBr-NF can be determined to -0.57 V and -0.53 V respectively based on the band gap formula ($E_g = E_{VB}\text{-}E_{CB}$). Thus, the electronic band structures of BiOBr and BiOBr-NF can be schemed on the basis of band gaps, valence band and conduction valence, as displayed in Fig. 5i.

ESR is utilized to assess the potential oxidation half-reaction. As displayed in Fig. 6a, no signal is observed under dark condition. Upon irradiation, the characteristic peaks of hydroxyl radical (·OH) are detected. These findings provide further support for the notion that the E_{VB} of BiOBr-NF has a higher positive potential than $\varphi_{OH/\cdot OH}$. Consequently, photoexcited VB holes are thermodynamicclly favorable for oxidizing H_2O, leading to the release protons and O_2. This verifies the corresponding oxidation and reduction steps in the N_2 reduction process:

$$2H_2O + h^+ \rightarrow O_2 + 4H^+$$

$$N_2 + 6H^+ + 6e^- \rightarrow 2NH_3$$

.

Overall reaction:

$$2N_2 + 6H_2O \rightarrow 4NH_3 + 3O_2$$

.
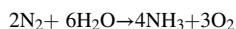
A proposed mechanism for the potential reduction of N_2 over Ru-BiOBr-NF is presented in Fig. 6b. In the aqueous, N_2 molecules are enriched on Ru-BiOBr-NF, thanks to the nanoconfined structure. Beneficiating from the exposed synergistic active sites of O defects and Ru, N_2 molecules are chemically adsorbed on the surface of Ru-BiOBr-NF. The unoccupied d-orbitals of Ru species accept the lone pair of electrons from dinitrogen via σ donation, thereby facilitating the activation of N_2 molecules. Upon irradiation, the photogenerated holes in the VB oxidize H_2O into O_2 and active protons. Simultaneously, electrons accumulated in the CB reduce the chemically adsorbed N_2 into NH_3.

4. Conclusions

In conclusion, we have developed a Ru-modified BiOBr nanoflower with oxygen defects for the efficient photoreduction of N_2 into NH_3. The optimal NH_3 generation rate for Ru-BiOBr-NF reaches 121.97 µmol g^{-1} h^{-1}, which is 6.1 and 2.8 times higher than that of pristine BiOBr-NS and Ru modified BiOBr without O defects, respectively. Both experimental analysis and theoretical calculations reveal that the enhanced photocatalytic activity can be attributed to the following effects: The porous nanoflower structure with confined inner space is efficient for inhibiting the free diffusion of N_2, facilitates the enrichment of N_2 molecules on the surface. The designed Ru-O defects serve as active units, in which, O defects are beneficial for the chemisorption of N_2 molecules, while RuO$_2$ adjusts electronic structures of BiOBr-NF, leading to the promotion of N_2 activation and lowering of the energy barriers of the rate-determining *N-N to *N-NH step. This work provides a general insight into the design of photocatalysts toward N_2 reduction via morphology and crystal structure regulation.

CRediT authorship contribution statement

Xia Yuzhou: Funding acquisition, Investigation, Methodology, Writing – original draft. **Xia Xinghe:** Investigation. **Chen Lu:** Methodology. **Liang Ruowen:** Supervision. **Yan Guiyang:** Funding acquisition, Supervision. **Liang Shijing:** Conceptualization, Funding acquisition, Supervision, Writing – review & editing.

Declaration of Competing Interest

The authors declare that they have no known competing financial interests or personal relationships that could have appeared to influence the work reported in this paper.

Data availability

Data will be made available on request.

Appendix A. Supporting information

Supplementary data associated with this article can be found in the online version at doi:10.1016/j.apcatb.2024.123859.

References

[1] Z. Chen, C. Liu, L. Sun, T. Wang, Progress of experimental and computational catalyst design for electrochemical nitrogen fixation, ACS Catal. 12 (2022) 8936–8975.

[2] W. Liao, K. Liu, J. Wang, A. Stefancu, Q. Chen, K. Wu, Y. Zhou, H. Li, L. Mei, M. Li, J. Fu, M. Miyauchi, E. Cortes, M. Liu, Boosting nitrogen activation via Ag nanoneedle arrays for efficient ammonia synthesis, ACS Nano 17 (2023) 411–420.

[3] G. Zhang, Y. Li, C. He, X. Ren, P. Zhang, H. Mi, Recent progress in 2D catalysts for photocatalytic and electrocatalytic artificial nitrogen reduction to ammonia, Adv. Energy Mater. 11 (2021) 2003294.

[4] N. Zhang, A. Jalil, D. Wu, S. Chen, Y. Liu, C. Gao, W. Ye, Z. Qi, H. Ju, C. Wang, X. Wu, L. Song, J. Zhu, Y. Xiong, Refining defect states in W$_{18}$O$_{49}$ by Mo doping: a strategy for tuning N$_2$ activation towards solar-driven nitrogen fixation, J. Am. Chem. Soc. 140 (2018) 9434–9443.

[5] T.N. Ye, S.W. Park, Y. Lu, J. Li, J. Wu, M. Sasase, M. Kitano, H. Hosono, Dissociative and associative concerted mechanism for ammonia synthesis over Co-based catalyst, J. Am. Chem. Soc. 143 (2021) 12857–12866.

[6] B.H.R. Suryanto, H.-L. Du, D. Wang, J. Chen, A.N. Simonov, D.R. MacFarlane, Challenges and prospects in the catalysis of electroreduction of nitrogen to ammonia, Nat. Catal. 2 (2019) 290–296.

[7] W. Liao, H.-X. Liu, L. Qi, S. Liang, Y. Luo, F. Liu, X. Wang, C.-R. Chang, J. Zhang, L. Jiang, Lithium/bismuth co-functionalized phosphotungstic acid catalyst for promoting dinitrogen electroreduction with high Faradaic efficiency, Cell Rep. Phys. Sci. 2 (2021) 100557.

[8] M. Xie, F. Dai, H. Guo, P. Du, X. Xu, J. Liu, Z. Zhang, X. Lu, Improving electrocatalytic nitrogen selectivity and yield by suppressing hydrogen evolution reaction via electronic metal-support interaction, Adv. Energy Mater. 13 (2023) 2203032.

[9] Y. Liu, L. Wang, L. Chen, H. Wang, A.R. Jadhav, T. Yang, Y. Wang, J. Zhang, A. Kumar, J. Lee, V.Q. Bui, M.G. Kim, H. Lee, Unveiling the protonation kinetics-dependent selectivity in nitrogen electroreduction: achieving 75.05% selectivity, Angew. Chem. Int. Ed. 61 (2022) e202209555.

[10] T. He, A.R.P. Santiago, A. Du, Atomically embedded asymmetrical dual-metal dimers on N-doped graphene for ultra-efficient nitrogen reduction reaction, J. Catal. 388 (2020) 77–83.

[11] Y. Wan, H. Zhou, M. Zheng, Z. Huang, F. Kang, F. Kang, J. Li, R. Lv, Oxidation state modulation of bismuth for efficient electrocatalytic nitrogen reduction to ammonia, Adv. Funct. Mater. 31 (2021) 2100300.

[12] R. Shi, Y. Zhao, G.I.N. Waterhouse, S. Zhang, T. Zhang, Defect engineering in photocatalytic nitrogen fixation, ACS Catal. 9 (2019) 9739–9750.

[13] Y. Zhang, L. Ran, Y. Zhang, P. Zhai, Y. Wu, J. Gao, Z. Li, B. Zhang, C. Wang, Z. Fan, X. Zhang, J. Cao, D. Jin, L. Sun, J. Hou, Two-dimensional defective boron-doped niobic acid nanosheets for robust nitrogen photofixation, ACS Nano 15 (2021) 17820–17830.

[14] J. Di, J. Xia, M.F. Chisholm, J. Zhong, C. Chen, X. Cao, F. Dong, Z. Chi, H. Chen, Y. X. Weng, J. Xiong, S.Z. Yang, H. Li, Z. Liu, S. Dai, Defect-tailoring mediated electron-hole separation in single-unit-cell Bi$_3$O$_4$Br nanosheets for boosting photocatalytic hydrogen evolution and nitrogen fixation, Adv. Mater. 31 (2019) e1807576.

[15] P. Li, Z. Zhou, Q. Wang, M. Guo, S. Chen, J. Low, R. Long, W. Liu, P. Ding, Y. Wu, Y. Xiong, Visible-Light-driven nitrogen fixation catalyzed by Bi$_5$O$_7$Br nanostructures: Enhanced performance by oxygen vacancies, J. Am. Chem. Soc. 142 (2020) 12430–12439.

[16] H. Zhang, Y. Chen, L. Bao, Y. Yuan, Double quantum dots decorated layer structure CeCO$_3$OH for improved N$_2$ photo-fixation, J. Catal. 412 (2022) 1–9.

[17] P. Li, S. Gao, Q. Liu, P. Ding, Y. Wu, C. Wang, S. Yu, W. Liu, Q. Wang, S. Chen, Recent progress of the design and engineering of bismuth oxyhalides for photocatalytic nitrogen fixation, Adv. Energy Sustain. Res 2 (2021) 2000097.

[18] Y. Zhao, Y. Zhao, R. Shi, B. Wang, G. Waterhouse, L. Wu, C. Tung, T. Zhang, Tuning oxygen vacancies in ultrathin TiO$_2$ nanosheets to boost photocatalytic nitrogen fixation up to 700 nm, Adv. Mater. 31 (2019) 1806482.

[19] Q. Han, C. Wu, H. Jiao, R. Xu, Y. Wang, J. Xie, Q. Guo, J. Tang, Rational design of high-concentration Ti^{3+} in porous carbon-doped TiO$_2$ nanosheets for efficient photocatalytic ammonia synthesis, Adv. Mater. 33 (2021) e2008180.

[20] D. Li, Y. Zhao, Y. Miao, C. Zhou, L. Zhang, L. Wu, T. Zhang, Accelerating electron-transfer dynamics by TiO$_2$-immobilized reversible single-atom copper for enhanced artificial photosynthesis of urea, Adv. Mater. 34 (2022) 2207793.

[21] Y. Liu, Z. Hu, J.C. Yu, Fe Enhanced visible-light-driven nitrogen fixation on BiOBr nanosheets, Chem. Mater. 32 (2020) 1488–1494.

[22] X. Xue, R. Chen, C. Yan, Y. Hu, W. Zhang, S. Yang, L. Ma, G. Zhu, Z. Jin, Efficient photocatalytic nitrogen fixation under ambient conditions enabled by the heterojunctions of n-type Bi$_2$MoO$_6$ and oxygen-vacancy-rich p-type BiOBr, Nanoscale 11 (2019) 10439–10445.

[23] X. Hui, L. Li, Q. Xia, S. Hong, L. Hao, A.W. Robertson, Z. Sun, Interface engineered Sb$_2$O$_3$/W$_{18}$O$_{49}$ heterostructure for enhanced visible-light-driven photocatalytic N$_2$ reduction, Chem. Eng. J. 438 (2022) 135485.

[24] Y. Zhao, L. Zheng, R. Shi, S. Zhang, X. Bian, F. Wu, X. Cao, G. Waterhouse, T. Zhang, Alkali etching of layered double hydroxide nanosheets for enhanced photocatalytic N$_2$ reduction to NH$_3$, Adv. Energy Mater. 10 (2020) 2002199.

[25] T. Wang, C. Feng, J. Liu, D. Wang, H. Hu, J. Hu, Z. Chen, G. Xue, Bi$_2$WO$_6$ hollow microspheres with high specific surface area and oxygen vacancies for efficient photocatalysis N$_2$ fixation, Chem. Eng. J. 414 (2021) 128827.

[26] D. Zhang, J. Li, Q. Wang, Q. Wu, High {001} facets dominated BiOBr lamellas: facile hydrolysis preparation and selective visible-light photocatalytic activity, J. Mater. Chem. A 1 (2013) 8622.

[27] G. Ren, M. Shi, Z. Li, Z. Zhang, X. Meng, Electronic metal-support interaction via defective-induced platinum modified BiOBr for photocatalytic N$_2$ fixation, Appl. Catal., B 327 (2023) 122462.

[28] H. Li, J. Shang, Z. Ai, L. Zhang, Efficient visible light nitrogen fixation with BiOBr nanosheets of oxygen vacancies on the exposed {001} facets, J. Am. Chem. Soc. 137 (2015) 6393–6399.

[29] X. Chen, X. Zhang, Y.-H. Li, M.-Y. Qi, J.-Y. Li, Z.-R. Tang, Z. Zhou, Y.-J. Xu, Transition metal doping BiOBr nanosheets with oxygen vacancy and exposed {102} facets for visible light nitrogen fixation, Appl. Catal., B 281 (2021) 119516.

[30] L. Zhang, F. Xie, J. Liu, Z. Sun, X. Zhang, Y. Wang, Y. Wang, R. Li, C. Fan, Light-switchable oxygen vacancies enhanced nitrogen fixation performance on BiOBr: Mechanism of formation, reconversion and function, Chem. Eng. J. 450 (2022) 138066.

[31] H. Li, M. Xia, B. Chong, H. Xiao, B. Zhang, B. Lin, B. Yang, G. Yang, Boosting photocatalytic nitrogen fixation via constructing low-oxidation-state active sites in the nanoconfined spinel iron cobalt oxide, ACS Catal. 12 (2022) 10361–10372.

[32] Z. Li, Z. Gao, B. Li, L. Zhang, R. Fu, Y. Li, X. Mu, L. Li, Fe-Pt nanoclusters modified Mott-Schottky photocatalysts for enhanced ammonia synthesis at ambient conditions, Appl. Catal., B 262 (2020) 118276.

[33] Z. Shang, B. Song, H. Li, H. Zhang, F. Feng, J. Kaelin, W. Zhang, B. Xie, Y. Cheng, K. Lu, Q. Chen, Atomically dispersed manganese Lewis acid sites catalyze electrohydrogenation of nitrogen to ammonia, CCS Chem. 4 (2022) 2115–2126.

[34] B. Hu, B.-H. Wang, L. Chen, Z.-J. Bai, W. Zhou, J.-K. Guo, S. Shen, T.-L. Xie, C.-T. Au, L.-L. Jiang, S.-F. Yin, Electronic modulation of the interaction between Fe single atoms and WO$_{2.72-x}$ for photocatalytic N$_2$ reduction, ACS Catal. 12 (2022) 11860–11869.

[35] Q. Meng, C. Lv, J. Sun, W. Hong, W. Xing, L. Qiang, G. Chen, X. Jin, High-efficiency Fe-mediated Bi$_2$MoO$_6$ nitrogen-fixing photocatalyst: Reduced surface work function and ameliorated surface reaction, Appl. Catal., B 256 (2019) 117781.

[36] L. Li, Y. Wang, S. Vanka, X. Mu, Z. Mi, C.J. Li, Nitrogen photofixation over III-nitride nanowires assisted by ruthenium clusters of low atomicity, Angew. Chem. Int. Ed. 56 (2017) 8701–8705.

[37] Y. Zhang, Q. Wang, S. Yang, H. Wang, D. Rao, T. Chen, G. Wang, J. Lu, J. Zhu, S. Wei, X. Zheng, J. Zeng, Tuning the interaction between ruthenium single atoms and the second coordination sphere for efficient nitrogen photofixation, Adv. Funct. Mater. 32 (2022) 2112452.

[38] G. Ren, J. Zhao, Z. Zhao, Z. Li, L. Wang, Z. Zhang, C. Li, X. Meng, Defects-induced single-atom anchoring on metal-organic frameworks for high-efficiency photocatalytic nitrogen reduction, Angew. Chem. Int. Ed. 63 (2024) e202314408.

[39] L. Wen, K. Sun, X. Liu, W. Yang, L. Li, H.L. Jiang, Electronic state and microenvironment modulation of metal nanoparticles stabilized by MOFs for boosting electrocatalytic nitrogen reduction, Adv. Mater. 35 (2023) e2210669.

[40] L.W. Chen, Y.C. Hao, Y. Guo, Q. Zhang, J. Li, W.Y. Gao, L. Ren, X. Su, L. Hu, N. Zhang, S. Li, X. Feng, L. Gu, Y.W. Zhang, A.X. Yin, B. Wang, Metal-organic framework membranes encapsulating gold nanoparticles for direct plasmonic photocatalytic nitrogen fixation, J. Am. Chem. Soc. 143 (2021) 5727–5736.

[41] W. Liao, L. Qi, Y. Wang, J. Qin, G. Liu, S. Liang, H. He, L. Jiang, Interfacial engineering promoting electrosynthesis of ammonia over Mo/phosphotungstic acid with high performance, Adv. Funct. Mater. (2021) 2009151.

[42] J. Zheng, Y. Lyu, M. Qiao, R. Wang, Y. Zhou, H. Li, C. Chen, Y. Li, H. Zhou, S. P. Jiang, S. Wang, Photoelectrochemical synthesis of ammonia on the aerophilic-hydrophilic heterostructure with 37.8% efficiency, Chem 5 (2019) 617–633.

[43] J. Li, G. Chen, Y. Zhu, Z. Liang, A. Pei, C.-L. Wu, H. Wang, H.R. Lee, K. Liu, S. Chu, Y. Cui, Efficient electrocatalytic CO$_2$ reduction on a three-phase interface, Nat. Catal. 1 (2018) 592–600.

[44] R. Guan, D. Wang, Y. Zhang, C. Liu, W. Xu, J. Wang, Z. Zhao, M. Feng, Q. Shang, Z. Sun, Enhanced photocatalytic N$_2$ fixation via defective and fluoride modified TiO$_2$ surface, Appl. Catal., B 282 (2021) 119580.

[45] M. Shang, W. Wang, L. Zhang, Preparation of BiOBr lamellar structure with high photocatalytic activity by CTAB as Br source and template, J. Hazard. Mater. 167 (2009) 803–809.

[46] X. Wu, Y.H. Ng, L. Wang, Y. Du, S.X. Dou, R. Amal, J. Scott, Improving the photo-oxidative capability of BiOBr via crystal facet engineering, J. Mater. Chem. A 5 (2017) 8117–8124.

[47] Y. Jin, F. Li, T. Li, X. Xing, W. Fan, L. Zhang, C. Hu, Enhanced internal electric field in S-doped BiOBr for intercalation, adsorption and degradation of ciprofloxacin by photoinitiation, Appl. Catal., B 302 (2021) 120824.

[48] J. Wu, X. Li, W. Shi, P. Ling, Y. Sun, X. Jiao, S. Gao, L. Liang, J. Xu, W. Yan, C. Wang, Y. Xie, Efficient visible-light-driven CO$_2$ reduction mediated by defect-engineered BiOBr atomic layers, Angew. Chem. Int. Ed. 57 (2018) 8719–8723.

[49] L. Su, Y. Jin, D. Gong, X. Ge, W. Zhang, X. Fan, W. Luo, The role of discrepant reactive intermediates on Ru-Ru$_2$P heterostructure for pH-universal hydrogen oxidation reaction, Angew. Chem. Int. Ed. 62 (2023) e202215585.

[50] F. Lei, Y. Sun, K. Liu, S. Gao, L. Liang, B. Pan, Y. Xie, Oxygen vacancies confined in ultrathin indium oxide porous sheets for promoted visible-light water splitting, J. Am. Chem. Soc. 136 (2014) 6826–6829.

[51] L. Hao, L. Huang, Y. Zhang, T. Ma, Oxygen vacant semiconductor photocatalysts, Adv. Funct. Mater. 31 (2021) 2100919.

[52] J. Wang, Y. Zhang, T. Zhou, S. Chen, H. Zhu, J. Bai, J. Li, B. Zhou, Efficient WO$_{3-x}$ nanoplates photoanode based on bidentate hydrogen bonds and thermal reduction of ethylene glycol, Chem. Eng. J. 404 (2021) 127089.

[53] M. Yu, Y. Chen, M. Gao, G. Huang, Q. Shan, J. Bi, Interspersed Bi promoting hot electron transfer of covalent organic frameworks boosts nitrogen reduction to ammonia, Small 19 (2023) 2206407.

[54] Y. Huang, Y. Zhu, S. Chen, X. Xie, Z. Wu, N. Zhang, Schottky junctions with Bi cocatalyst for taming aqueous phase N$_2$ reduction toward enhanced solar ammonia production, Adv. Sci. 8 (2021) 2003626.

[55] T. He, Z. Zhao, R. Liu, X. Liu, B. Ni, Y. Wei, Y. Wu, W. Yuan, H. Peng, Z. Jiang, Y. Zhao, Porphyrin-based covalent organic frameworks anchoring Au single atoms for photocatalytic nitrogen fixation, J. Am. Chem. Soc. 145 (2023) 6057–6066.

[56] X.-H. Li, H. Li, S.-L. Jiang, L. Yang, H.-Y. Li, Q.-L. Liu, W. Bai, Q. Zhang, C. Xiao, Y. Xie, Constructing mimic-enzyme catalyst: Polyoxometalates regulating carrier dynamics of metal-organic frameworks to promote photocatalytic nitrogen fixation, ACS Catal. 13 (2023) 7189–7198.

[57] T. He, Z. Zhao, R. Liu, X. Liu, B. Ni, Y. Wei, Y. Wu, W. Yuan, H. Peng, Z. Jiang, Y. Zhao, Porphyrin-based covalent organic frameworks anchoring Au single atoms for photocatalytic nitrogen fixation, J. Am. Chem. Soc. 145 (2023) 6057–6066.

[58] Y. Zhao, Y. Zhao, G. Waterhouse, L. Zheng, X. Cao, F. Tang, L. Wu, C. Tung, D. Hare, T. Zhang, Layered-double-hydroxide nanosheets as efficient visible-light-driven photocatalysts for dinitrogen fixation, Adv. Mater. 29 (2017) 1703828.